

## Numerical Transient Thermal Development of Melting a Solid Filament in A Hot-End of a Material Extrusion System.

Gaius Chukwuka Nzebuka <sup>a</sup>, Chukwuzubelu Okenwa Ufodike <sup>a\*</sup>

<sup>a</sup>Department of Engineering Technology and Industrial Distribution, Texas A&M University,  
3367 TAMU, College Station, TX 77843 United States.

\*Corresponding author. E-mail: [ufodike@tamu.edu](mailto:ufodike@tamu.edu)

### Abstract

Additive manufacturing of polymer feedstock in the form of solid filament is challenging due to heat transfer limitations. The ease of melting the filament in the liquefier influences the production rate and life cycle of the hot-end components. This study presents numerical transient thermal development during the melting of the solid filament in the liquefier. The sample filament material selected for the study is a tough polylactic acid (TPLA). The transient computation of thermal distribution and liquid fraction evolution was performed using computational fluid dynamics (CFD) commercial software. However, the numerical model formulations cannot be directly applied to the available CFD software. Therefore, a user-defined function (UDF) was written and interfaced with the CFD software for the properties field-dependent functions. Special care was taken to capture the motion of the solid filament by patching the velocity explicitly in the flow domain. One simulation was performed without accounting for the velocity of the translating solid filament and the result obtained revealed that the case that accounts for the velocity of the solid filament predicts the infrared thermographic measured nozzle exit temperature of the extrudate more accurately. Also, a steady thermal development was achieved in the hot end after 25 seconds. The transient thermal analysis can be useful for a better understanding of melting dynamics in the liquefier and assist in process control planning.

**Keywords:** Temperature; Melting; Push Velocity; Numerical; Modeling

### 1. Introduction

Material extrusion additive manufacturing is a process of shaping complex 3D dimensional parts by pushing molten material through a small capillary (nozzle outlet) and depositing the melted material layer by layer on a preheated movable platform. If the feedstock used is in the form of a spooled polymer filament, the process is called fused filament fabrication (FFF). The feedstock can also be in the form of pellets or granules of polymers. FFF begins by pushing the polymer filament with a diameter of 1.75 mm or 2.85 mm through a pinch-roller mechanism into the liquefier [1]. The liquefier is a rectangular metal (commonly aluminum) block equipped with an electrical resistance heating coil that provides the thermal energy necessary to completely melt the filament. The amount of melt in the liquefier usually depends on the heat flux and material feed rate, among other factors [1]. The pressure necessary to maintain the flow of the molten polymer through the nozzle is provided upstream from the unmelted solid part of the filament that acts as a continuous piston. The pressure and other flow variables such as temperature, velocity, and liquid fraction evolution that affect the performance of the liquefier can be determined using predictive computational modeling tools.

Computational fluid dynamics (CFD) are a reliable predictive tool that have recently been employed to model the flow variable interactions inside the liquefier [1-9]. The CFD modeling tool is handy because it complements the experimental method and provides the valuable insight needed for an improved understanding of complex physics during the melting of the polymer filament. For example, to optimize the size of the stepper motor that drives the feeding mechanism, knowledge about the feeding force and pressure drop during extrusion is necessary. The extrusion pressure can only be predicted accurately using a numerical approach to generate a sufficient pressure data map. The measurement of the pressure at every location in the liquefier using experimental and analytical techniques is impossible and can produce inaccurate results [10, 11]. Also, the temperature distribution and liquid evolution in the hot-end (i.e., the geometrical arrangement of the liquefier and the nozzle) can only be visualized with sufficient qualitative and quantitative transient information using the numerical method.

The evolution of temperature and liquid fraction with time as the heating of the filament proceeds helps in understanding the liquefier thermal loading response. Understanding the liquefier thermal response can be useful in the process planning, control, and possible redesigning of the hot-end for rapid melting of the polymer filament with a reduced production time. As a result, a need is created for a high-fidelity numerical tool to capture the relevant physical phenomena in the hot-end. Recently [4, 5, 7-9, 12] have employed the CFD model to study the complex flow physics in the hot-end. Their models used the filament feeding rate as inlet velocity without explicitly accounting for the push filament velocity inside the liquefier. The push velocity described the translational motion of the solid filament upstream within the liquefier and the relative motion between liquid and solid in the melting zone.

Therefore, the design of the current work is to capture the push velocity of the filament that provides the required pressure needed for material extrusion of the polymer. The study will present the evolution of temperature and liquid fraction at different times as a function of the radial distance from the outlet. It is expected that the new understanding provided by the current work will further provide CFD and design engineers with more tools necessary for modeling the FFF system.

## **2. Experimental Methods**

### **2.1. Materials and primary equipment**

All experimental testing were performed with tough-poly(lactic acid) (TPLA) filament manufactured by Ultimaker 3D Products. A DSC2500 (TA instruments) test was conducted from -20 °C to 230 °C, with a heating rate of 5 °C/min to determine the glass transition temperature of TPLA and melting temperature. An Aluminium Tzero Hermetic pan (pan mass 50.1 mg) and lids were used to seal the testing samples of mass 5.2 mg.

### **2.2 Thermal characterization:**

#### **2.2.1 Differential Scanning Calorimetry**

A DSC test was performed to determine the melting temperature, melting enthalpy, and glass transition temperature. The temperature range obtained from the test shows where the glass-

like TPLA material takes the transition to a soft rubbery material. The upper-temperature limit was set to 503 K (230 °C) based on Thermogravimetric analysis (TGA) to avoid sample degradation within the chamber. The temperature precision and accuracy of the instrument were  $\pm 0.01$  °C and  $\pm 0.1$  °C, respectively. The thermal diffusivity and specific heat capacity were measured using the DFX-900 Xenon flash diffusivity analyzer (TA instruments). Three samples of dimensions 12.7 mm diameter and 5 mm thickness were tested. The procedure involves heating the sample with a nearly uniform pulse across the face. The test was conducted in a nitrogen environment, and the sample was heated from 20 to 140 °C. The thermal conductivity was calculated using the product of thermal diffusivity, specific heat capacity, and density relation.

The viscosity of the TPLA was measured using a TA Instruments ARES-G2 rheometer (TA Instruments, Inc., New Castle, USA) with a 25 mm parallel plate geometry and a gap width of 1 mm. First, an amplitude sweeps at 473 K (200 °C), and a frequency of 10 rad/s was run to estimate the linear viscoelastic regime (LVR). Secondly, a frequency sweeps with strain amplitudes of 0.1 to 628 rad/s at 443 K (170 °C), 463 K (190 °C), 483 K (210 °C), and 503 K (230 °C). The time-temperature superposition at 463 K (190 °C) and the Cox-Merz rule were used to obtain the steady shear viscosity.

### 3.0 Numerical description

The Generalized Newtonian incompressible 2D axisymmetric flow and viscous dissipation are considered. The melting model presented in [8] is used with the assumption that the liquid fraction ( $f_l$ ) is approximated with a linear temperature relation  $f_l = \frac{T-T_s}{T_m-T_s}$ . The  $T_m$  is the melting temperature and its value is determined by the DSC test, which is provided in the next section. The  $T_s$  is the solidus temperature and is also determined from the Xenon flash analysis.

#### 3.1 Governing equations and Boundary Conditions

$$\nabla(\rho\vec{V}) = 0 \quad (1)$$

$$\frac{\partial}{\partial t}(\rho\vec{V}) + \nabla(\rho\vec{V}\vec{V}) = -\nabla P + \nabla\left(\eta\frac{\rho}{\rho_l}\nabla\vec{V}\right) - \frac{\rho}{\rho_l}\frac{\eta}{K}\cdot(\vec{V} - \vec{V}_p) - \rho_l\beta_l(T - T_l)\vec{g} \quad (2)$$

$$\begin{aligned} \frac{\partial}{\partial t}(\rho c_p T) + \nabla(\rho c_p \vec{V} T) &= \nabla(k\nabla T) - \nabla(\rho f_s L(\vec{V} - \vec{V}_s)) - \nabla(\rho f_l \vec{V} L) - \frac{\partial}{\partial t}(\rho f_l L) + \\ \eta\left(\frac{\partial v_i}{\partial x_j} + \frac{\partial v_j}{\partial x_i}\right)\frac{\partial v_i}{\partial x_j} & \end{aligned} \quad (3)$$

where  $\rho$  is the density,  $\vec{V}$  is the velocity vector,  $\eta$  is the dynamic viscosity,  $K$  is the permeability,  $\vec{V}_p$  is the push velocity vector (in the current work, the push velocity is vertically downward),  $\beta_l$  is the coefficient of the thermal expansion,  $\vec{g}$  is the acceleration due to gravity vector,  $c_p$  is the specific heat capacity,  $f$  is the mass fraction,  $L$  is the latent heat of fusion (or melting enthalpy), the subscripts  $l$  and  $s$  represent the liquid and solid phases, respectively,  $t$  is the time, and  $k$  is the thermal conductivity. The interpretation of various terms in Eqs. (3 and 4) is well described in [8].

Fig. 1 is a schematic illustration of the computational domain with indicated dimensions and boundary sections.

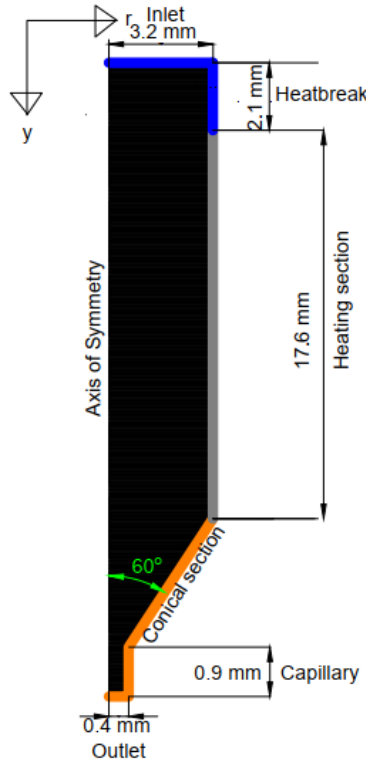


Fig. 1 The Computational domain with associated boundary sections

The diameter of the filament is 2.85 mm and enters the domain at room temperature as a rigid solid with a prescribed feeding rate (velocity). A slip boundary condition was imposed at the heatbreak sections and a no-slip condition was applied at the heating, conical, and capillary sections. The filament is heated as it travels down the liquefier channel with heat flux defined by Eq. (4):

$$q_{mixed} = q_{conv} + q_{rad} = h(T_w - T_\infty) + \frac{\sigma(T_w^4 - T_\infty^4)}{\varphi} \quad (4)$$

$$h = h_{gap}f_s + h_c f_l \quad (5)$$

where  $q_{conv}$  and  $q_{rad}$  is convective and radiative heat fluxes, respectively,  $\sigma$  is the Stefan-Boltzmann constant,  $T_w$  is a known wall temperature,  $T_\infty$  is the unknown surface temperature of the polymer ( $T_\infty = T$  during iteration at the boundary surface) which is to be predicted numerically, and  $\varphi$  is written as given in [4]:

$$\varphi = \frac{1}{\varepsilon_f} + \frac{1 - \varepsilon_b}{\varepsilon_b} \frac{r_f}{r_b} \quad (6)$$

where  $\varepsilon_f$  (0.92, [7]) and  $\varepsilon_b$  (0.60, [13]) are the emissivity of the filament and the heat break respectively,  $r_f$  and  $r_b$  are the radius of the filament and the heat break respectively. Zero shear stress was specified on the wall of the heat break region.

The  $h_{gap}$  is the heat transfer coefficient in the air gap between the filament and the liquefier wall (barrel),  $h_c$  is the contact wall heat transfer coefficient,  $f_s$  and  $f_l$  are the solid and liquid fractions determined using a linear temperature relationship [14-17]. The respective values of the  $h_{gap}$  and  $h_c$  were systematically calibrated with measured feeding force data in [11] at a low feeding rate of 40 mm/min. The filament is expected to be fully liquid at nozzle exit with a flow boundary condition described in Eq. 7

$$P = -\rho g D_{nozzle} \quad (7)$$

The Carreau-Yasuda's and Arrhenius's relation for modeling the shear rate-temperature dependent viscosity is presented as follows;

$$\eta(\dot{\gamma}, T) = \eta(T)\eta(\dot{\gamma}) \quad (8)$$

where

$$\eta(T) = \exp\left[\frac{E_a}{R}\left(\frac{1}{T} - \frac{1}{T_{ref}}\right)\right] \quad (9)$$

$$\eta(\dot{\gamma}) = \eta_{inf} + (\eta_o - \eta_{inf})[1 + (\lambda\dot{\gamma})^a]^{n-1/a} \quad (10)$$

where  $\eta_o$  is the Newtonian plateau viscosity,  $\eta_{inf}$  infinite-shear rate viscosity,  $\eta$  is the dynamic viscosity,  $n$  is the power-law index,  $a$  is the index that controls the transition from the Newtonian plateau to the power-law region,  $\lambda$  is a time constant,  $E_a$  is the activation energy,  $R$  is the gas constant,  $T_{ref}$  is the reference temperature,  $T$  is the temperature, and  $\dot{\gamma}$  is the magnitude of the shear rate defined using the strain deformation tensor. The parameters of Eqs. 9 and 10 are given in Table 1.

**Table 1**  
Fitting Parameters for the Carreau-Yasuda's and Arrhenius's relation and physically measured properties of TPLA.

Variables	Unit	Value
$\eta_{inf}$	kg/m-s	5440
$\eta_o$	kg/m-s	-230
$\lambda$	s	0.052
$n$	-	0.398
$a$	-	0.72
$E_a$	kJ/mol	75.59
$T_{ref}$	K (°C)	463 (190)
$T_m$	K (°C)	423.89 (150)
$T_s$	K (°C)	414 (140)
$T_g$	K (°C)	334.78 (62)
$\rho$	kg/m <sup>3</sup>	1220
$L$	J/kg	120

The specific volume ( $1/\rho$ ) of the PLA during phase change is modeled using the Tait equation;

$$1/\rho(P, T) = (1/\rho)_o(t) \left[ 1 - 0.0894 \ln \left( 1 + \frac{P}{B(T)} \right) \right] + (1/\rho)_t(T, P) \quad (11)$$

$$\text{If } T > T_t$$

$$(1/\rho)_t(T, P) = 0 \quad (12)$$

$$(1/\rho)_o(t) = b_{1m} + b_{2m}T_b$$

$$B(T) = b_{3m} \exp[-b_{4m}T_b] \quad (13)$$

$$\text{If } T < T_t(P)$$

$$(1/\rho)_t(T, P) = b_7 \exp[b_8T_b - b_9P] \quad (14)$$

$$(1/\rho)_o(t) = b_{1s} + b_{2s}T_b \quad (15)$$

$$B(T) = b_{3s} \exp[-b_{4s}T_b] \quad (16)$$

where  $P$  is the pressure in Pa,  $T$  is the temperature in K,  $1/\rho$  is the specific volume in  $\text{m}^3/\text{kg}$ ,

$$T_t(P) = b_5 + b_6P \quad (17)$$

$$T_b = T - b_5 \quad (18)$$

The parameters in Eqs. 11-18 are given in [18] and are provided in the appendix.

The specific heat capacity determined from the Xenon flash diffusivity analysis is given by;

$$C_p [\text{J} \cdot \text{kg}^{-1} \cdot \text{K}^{-1}] = 3199.196 - 4.2343T + 0.03071T^2, \quad (19)$$

and the result of the thermal conductivity measurement indicates a weak temperature dependence; therefore, an average value of 0.645 W/m.k is used in the simulation.

### 3. 2. Solution Implementation

Fig. 2 shows the procedure used to implement the numerical solution. The grids were systematically refined to achieve a grid-independent solution, and the number of computational cells used in the calculation is 33822. The solution was initialized with the values of the inlet flow variables. Then, the computational cells were patched with the filament push velocity which corresponds to the feeding rate. The calculations were performed at 200 iterations for every step of 0.1 s to ensure convergence.

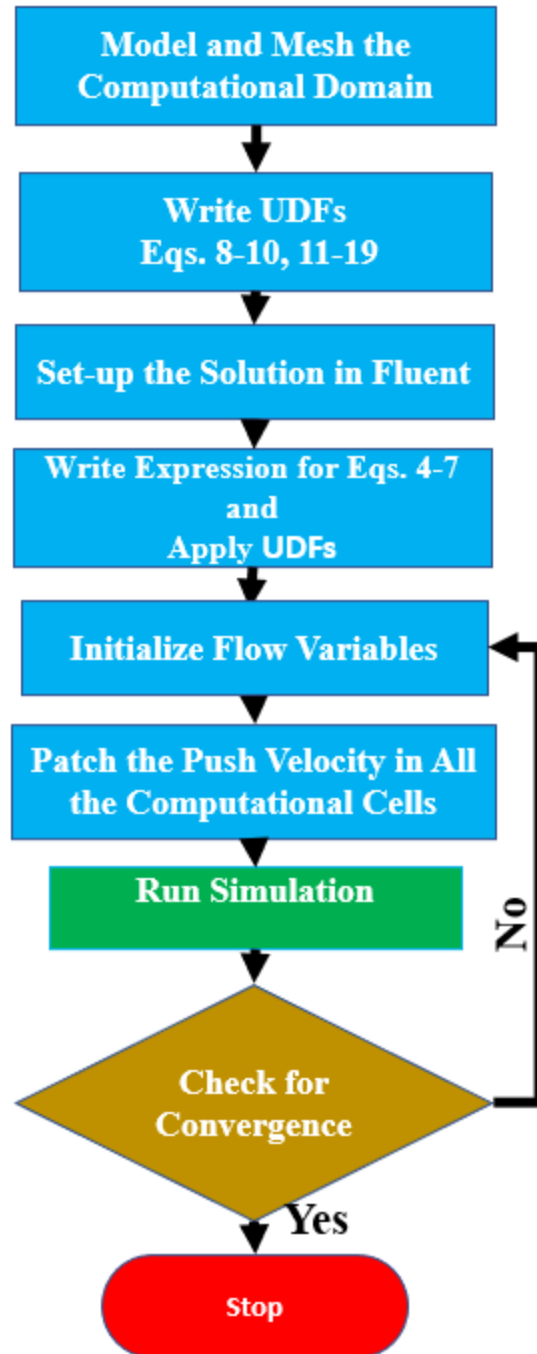


Fig. 2 The solution process for predicting thermal evolution in the hot-end

#### 4.0 Results and Discussion

To illustrate the benefit of including the push velocity in the computational domain, an additional simulation was run without capturing the push velocity. The results were compared with measured (measured with infrared thermography) extrudate temperature at the outlet. The

measurement was performed at a 40 mm/min feeding rate and a liquefier wall temperature of 503 K (230 °C).

The results obtained are presented in Table 3 which indicates that the predicted face averaged temperature of the extrudate at the nozzle outlet, for the case that includes the filament push velocity, is more accurate than the case without push velocity inclusion. The prediction of the outlet temperature observed with the inclusion of filament push velocity is better because it is a more realistic interpretation of the extra thermal energy required to melt the cold filament as it traveled down the liquefier barrel. Thus, it results in a lower outlet temperature than the case without push velocity.

Table 3 Comparison of the face average predicted and measured temperature

Cases	Extrudate Temperature (K)
Infrared measurement	472.44 K
Predicted with push velocity	471.80 K
Predicted without push velocity	475.16 K

Fig. 3 shows that this lower temperature prediction for the filament push velocity case occurred in the vicinity of the nozzle center. However, towards the nozzle walls, the predicted temperature is the same for the two cases.

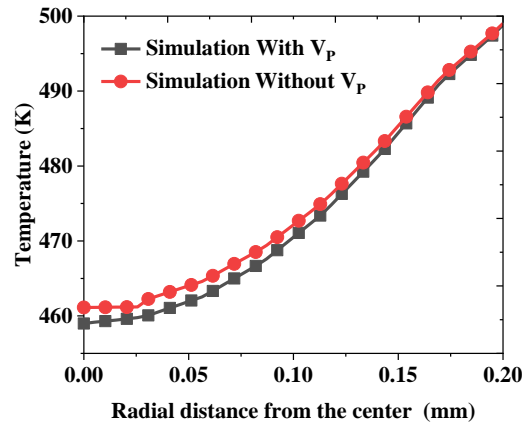


Fig. 3 Predicted average temperature at the nozzle outlet at  $t = 25$  s

#### 4.1 Transient thermal analysis of the numerical result

The transient response of the liquefier at the nozzle outlet is presented in Fig. 4. The simulation was performed with a liquefier wall temperature of 503 K, a feeding rate of 40 mm/min, and the temperature was recorded every 1 s. An additional simulation with a feeding rate of 60 mm/min was performed to illustrate the liquefier step response with a change in the filament velocity. Fig. 4a shows that at the initial time, the averaged outlet temperatures for the two feeding rate cases are the same. The outlet temperature rises immediately varying linearly with time above the glass transition temperature (334.78 K). It then widens above 1 s with a steep rise to 367.45 K. The predicted temperature for 40 mm/min is 382.06 K in 2 s. In comparison, 60 mm/min is 374.48

K in 2 s, recording a temperature difference of 7.58 K. A steady-state temperature was obtained in 25 s at a temperature of 471.80 K for the lower feeding rate. Contrastly, in 20 s, and at a temperature of 451.80 K, the higher feeding rate case attains a steady-state with a temperature difference of 20 K.

The predicted temperature for the lower feeding rate at the same time where the higher feeding rate reaches a steady-state is 465.57 K. A comparison of the temperature predicted at 20 s for the two cases gives a temperature difference of 13.77 K for the higher feeding rate. This indicates that the temperature difference between the two cases increases with time. But the increase in temperature difference between the two feeding rates is not in a linear fashion. Fig. 4a shows that the two curves are close to each other within 10 to 14 s and widen above 14 s. This shows that temperature and velocity have nonlinear relationship. The temperature and velocity are coupled in the melting governing equation through shear rate-temperature dependent viscosity relation and buoyance term in Eq. 2. However, the buoyance forces in the flow of a hot-end are insignificant [8]. Therefore, the nonlinear response of the transient thermal development at the nozzle outlet is only influenced via the shear rate-temperature-dependent viscosity relation (Eqs. 8-10).

Fig. 4b shows a step-change in the feeding rate at 25 s with an increase in the feeding rate to 60 mm/min. The curve undergoes a steep decrease and reaches a steady-state within 40 seconds.

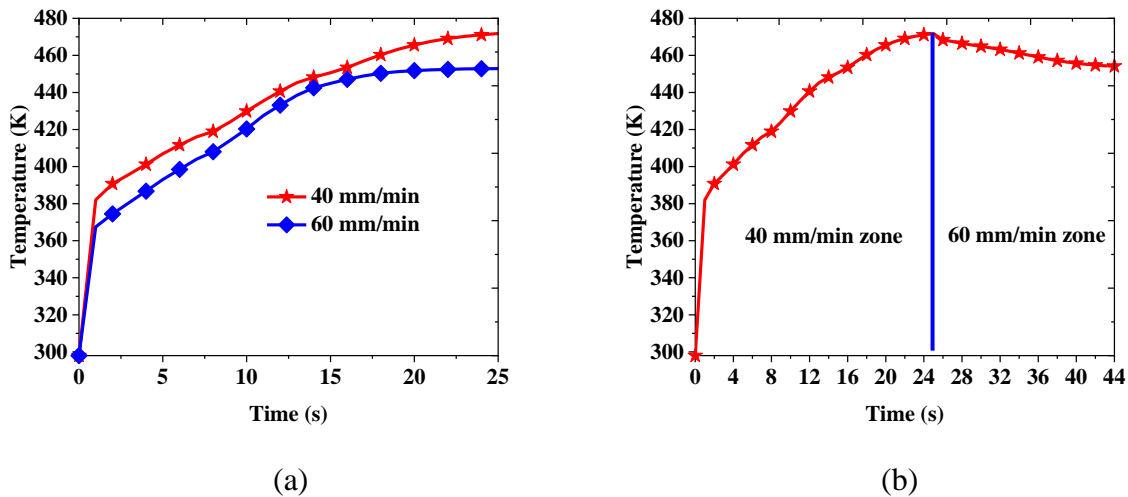


Fig. 4 Predicted averaged face temperature at the nozzle outlet as a function of time for (a) 40 and 60 mm/min from  $t = 0$  to 25 s (b) for a step-change in the feeding rate at  $t = 25$  s.

This implies that it took 15 s to reach a steady for 20 mm/min step change in the feeding rate. The drop in temperature at a higher feeding rate is associated with introducing new cold material at a higher feeding rate [19]. Suppose it is desired to increase the temperature back to its peak value of 471.80 K at a feeding rate of 60 mm/min. In that case, the heat input through the electrical resistance coils must be increased to compensate for the temperature difference.

Fig. 5 illustrates the radial variation of the outlet temperature at a different time for a feeding rate of 40 mm/min and liquefier wall temperature of 503 K. It is evident from the figure that the temperature curves increase upward as time progresses. The temperature curves for 25, 35, and 45 s coincided, emphasizing that steady was attained at 25 s for the feeding rate of 40 mm/min. The temperature curves increase from the center to the nozzle wall corresponding to the typical profile observed in the literature [4, 5, 7, 8]. This indicates that melting is lowest at the nozzle center and highest towards the nozzle wall, further revealed in Fig. 6.

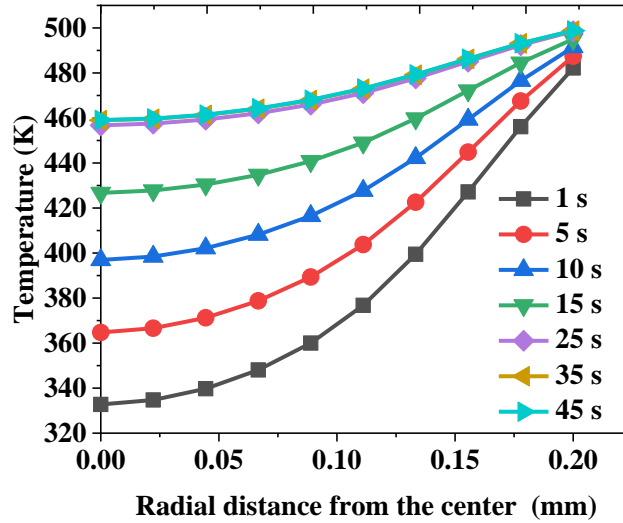


Fig. 5 Radial variation of temperature at the nozzle outlet for different time

Fig. 6 shows the transient liquid fraction contours superimposed with an isothermal glass transition temperature ( $T_g$ ) and melting temperature ( $T_m$ ) at different times (0 to 45 s). The color bar shows a different level of liquid fraction, red indicates fully liquid while blue indicates fully solid, and other colors suggest a compromise between solid and liquid. Initially, the hot-end is at room temperature (298 K), and the liquid fraction inside the liquefier is zero.

At  $t \leq 5$  s, film melting was evident in the conical wall section of the nozzle due to insufficient heating at a lower time. At  $t \leq 15$  s, the liquid fraction increases from the hot-end periphery towards the center and along the liquefier wall. The  $T_g$  isotherm reaches a steady-state at the central position and liquefier wall in 10 s. However, at  $t = 15$  s, a solid phase is still evident in the center of the conical section of the hot-end with an increased radial spread in the liquid fraction, and it establishes a steady position upstream of the liquefier wall. Fig. 6 again confirms that at  $t \geq 25$  s, melting attains a steady-state. Also,  $t \geq 25$  s, the liquid fraction and the  $T_m$  isotherm has established a nose-shape profile upstream of the liquefier center.

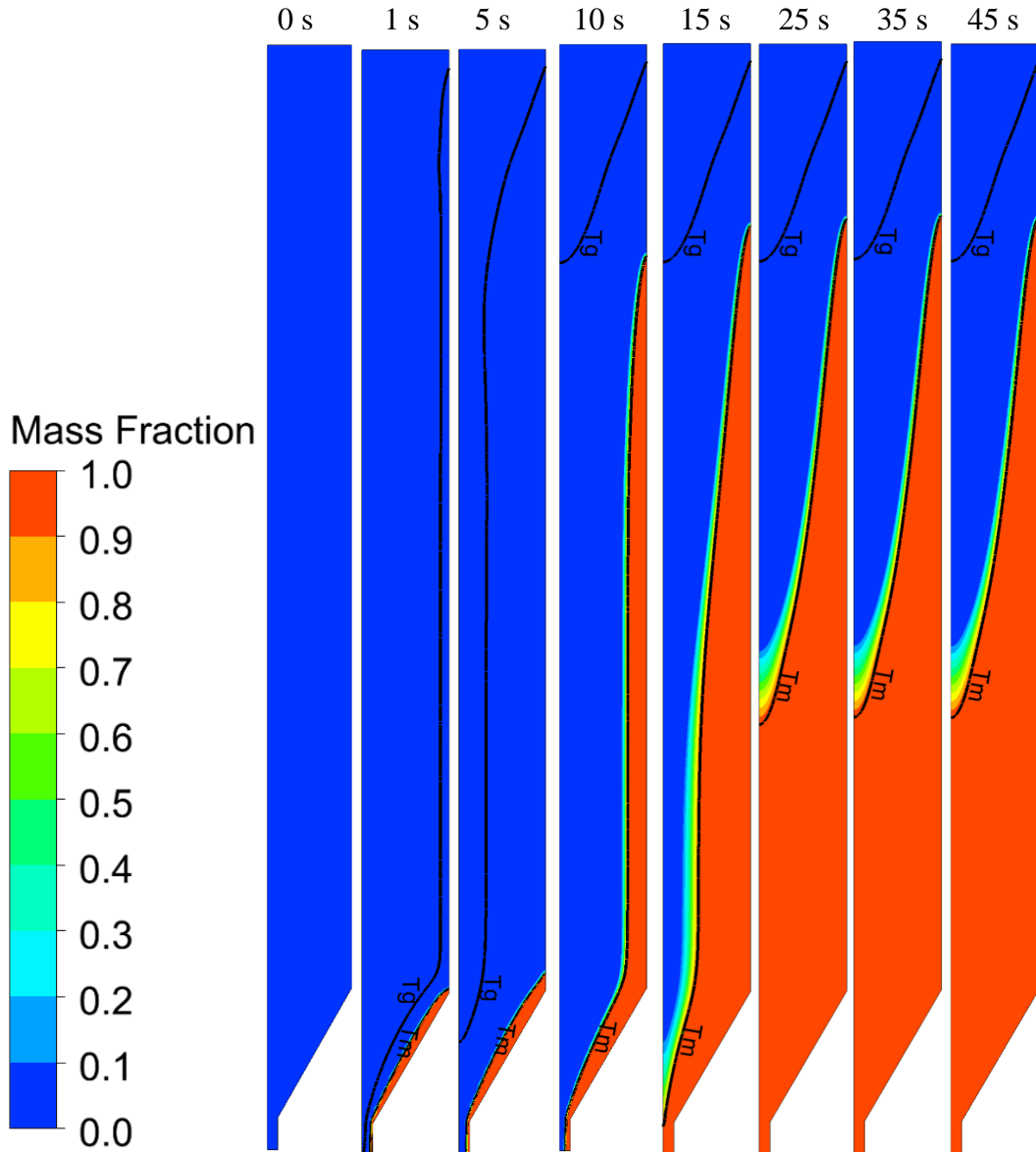


Fig. 6 Contour of liquid fraction development in the hot-end superimposed with two ( $T_g$  and  $T_m$ ) isothermal lines for different time

The liquid fraction profile suggests that heat transfer is from the liquefier wall to the center and that a good portion of the filament is still in the solid-state, thereby providing the needed pressure for extrusion. Hence, the result suggests that the polymer filament is not preheated to the melting point upstream of the liquefier, offering successful extrusion.

## 5. Conclusion

The current study provides a new understanding of the transient melting of polymer filament in the FFF system. The physical properties of the polymer were characterized and the

results presented. The melting model equations were used to solve the transient temperature and liquid fraction development in the liquefier. The push velocity of the filament was accounted for in the simulation. The following conclusion were derived from the simulation.

- The extrudate temperature at the outlet was better predicted than the condition without push velocity inclusion.
- Analysis at a feeding rate of 40 and 60 mm/min indicates a decrease in temperature at a higher feeding rate.
- A comparison of the two feeding rates shows that for 40 and 60 mm/min, a steady-state was attained at 25 and 20 s, respectively, and the differential temperature reported at steady-state is 20 K.
- The liquid fraction contours reveal a film melting at a lower time with an increase in the melting area as time progresses.
- The liquid fraction contour indicates that the filament is in a solid-state upstream of the liquefier which helps to maintain extrusion pressure.

The results obtained in this study are helpful for process parameter control in a condition where there is a step-change in the feeding rate. Also, more understanding of the transient melting dynamics of the liquefier was revealed using the numerical model. It is suggested that this model can be integrated for a possible redesign and upscaling process parameters in the hot-end of the FFF system.

## Appendix

Table A1 Parameters of the Tai Equation [18]

Parameter	Value	Unit
$b_{1s}$	0.000821	$m^3/kg$
$b_{2s}$	$4.469 \times 10^{-7}$	$m^3/kg$
$b_{3s}$	$2.142 \times 10^8$	Pa
$b_{4s}$	$6.079 \times 10^{-3}$	1/K
$b_{1m}$	$8.26 \times 10^{-4}$	$m^3/kg$
$b_{2m}$	$8.503 \times 10^{-7}$	$m^3/kg$
$b_{3m}$	$1.628 \times 10^8$	Pa
$b_{4m}$	$6.22 \times 10^{-3}$	1/K
$b_5$	348.15	K
$b_6$	$9.547 \times 10^{-8}$	K/Pa
$b_7$	0	$m^3/kg$
$b_8$	0	1/K
$b_9$	0	1/Pa
$\rho_l$	1072.7	$kg/m^3$

## References

1. Go, J., et al., Rate limits of additive manufacturing by fused filament fabrication and guidelines for high-throughput system design. Additive Manufacturing 2017. 16: p. 1-11.

2. Comminal, R., et al., Numerical modeling of the strand deposition flow in extrusion-based additive manufacturing. *Additive Manufacturing* 2018. 20: p. 68-76.
3. Comminal, R., et al., Motion planning and numerical simulation of material deposition at corners in extrusion additive manufacturing. *Additive Manufacturing* 2019. 29: p. 100753.
4. Kattinger, J., et al., Numerical simulation of the complex flow during material extrusion in fused filament fabrication. *Additive Manufacturing* 2022: p. 102476.
5. Pigeonneau, F., et al., Heating and flow computations of an amorphous polymer in the liquefier of a material extrusion 3D printer. *Additive Manufacturing* 2020. 32: p. 101001.
6. Ramanath, H., et al., Melt flow behaviour of poly- $\epsilon$ -caprolactone in fused deposition modelling. 2008. *Journal of Materials Science* 19(7): p. 2541-2550.
7. Serdeczny, M.P., et al., Numerical modeling of the polymer flow through the hot-end in filament-based material extrusion additive manufacturing. *Additive Manufacturing* 2020. 36: p. 101454.
8. Ufodike, C.O. and G.C. Nzebuka, Investigation of thermal evolution and fluid flow in the hot-end of a material extrusion 3D Printer using melting model. *Additive Manufacturing* 2022. 49: p. 102502.
9. Wang, P., et al., Effects of printing parameters of fused deposition modeling on mechanical properties, surface quality, and microstructure of PEEK. *Journal of Materials Processing Technology* 2019. 271: p. 62-74.
10. Phan, D.D., Z.R. Swain, and M.E. Mackay, Rheological and heat transfer effects in fused filament fabrication. *Journal of Rheology* 2018. 62(5): p. 1097-1107.
11. Serdeczny, M.P., et al., Experimental and analytical study of the polymer melt flow through the hot-end in material extrusion additive manufacturing. *Additive Manufacturing* 2020. 32: p. 100997.
12. Phan, D.D., et al., Computational fluid dynamics simulation of the melting process in the fused filament fabrication additive manufacturing technique. *Additive Manufacturing* 2020. 33: p. 101161.
13. Morgan, R.V., et al., Emissivity measurements of additively manufactured materials. 2017, Los Alamos National Lab.(LANL), Los Alamos, NM (United States).
14. Nzebuka, G.C., et al., Accounting for Melt Flow Pattern and Solid Fraction Evolution in DC Casting of Al-Cu Alloy Using v2f Turbulence Model. *Metallurgical and Materials Transactions B* 50 2019. 50(2): p. 866-880.
15. Nzebuka, G.C. and M.A. Waheed, Thermal evolution in the direct chill casting of an Al-4 pct Cu alloy using the low-Reynolds number turbulence model. *International Journal of Thermal Sciences* 2020. 147: p. 106152.
16. Nzebuka, G.C., U.O. Ufodike, C.P., Egole, Influence of various aspects of low-Reynolds number turbulence models on predicting flow characteristics and transport variables in a horizontal direct-chill casting. *International Journal of Heat and Mass Transfer*, 2021. 179: p. 121648.
17. Waheed, M.A., G.C. Nzebuka, and E.C.C. Enweremadu. Potent turbulence model for the computation of temperature distribution and eddy viscosity ratio in a horizontal direct-chill casting. *Num. Heat. Trans. Part A: Applications*, 2020. 79(4): p. 294-310.
18. Sin, L.T., et al., Comparison of injection molding processability of polylactic acid and high-density polyethylene via computational approach. *J. Poly. Sci.*, 2013. 33(2): p. 121-132.

19. Bellini, A., et al., Liquefier dynamics in fused deposition. *J. Manuf. Sci. Eng.* 2004. 126(2): p. 237-246.